

# UC Davis

## UC Davis Previously Published Works

### Title

Orthogonal analysis reveals inconsistencies in cargo loading of extracellular vesicles

### Permalink

<https://escholarship.org/uc/item/0b3504gk>

### Journal

Journal of Extracellular Biology, 3(8)

### ISSN

2768-2811

### Authors

Lowe, Neona M

Mizenko, Rachel R

Nguyen, Bryan B

et al.

### Publication Date



2024-08-01

### DOI

10.1002/jex2.70003

Peer reviewed

# Orthogonal analysis reveals inconsistencies in cargo loading of extracellular vesicles

Neona M. Lowe<sup>1</sup>  | Rachel R. Mizenko<sup>1</sup> | Bryan B. Nguyen<sup>1</sup> | Kwan Lun Chiu<sup>1</sup> | Vishalakshi Arun<sup>1</sup> | Alyssa Panitch<sup>1,2</sup> | Randy P. Carney<sup>1</sup> 

<sup>1</sup>Department of Biomedical Engineering, University of California, Davis, California, USA

<sup>2</sup>Wallace H. Coulter Department of Biomedical Engineering, Georgia Institute of Technology and Emory University, Atlanta, Georgia, USA

## Correspondence

Randy P. Carney, Department of Biomedical Engineering, University of California, Davis, CA, USA.

Email: rcarney@ucdavis.edu

## Funding information

NIH, Grant/Award Numbers: 1F31NS120590, R01CA241666, R01EB033389, R01EB034279, T32GM144303, T32HL007013

## Abstract

Since extracellular vesicles (EVs) have emerged as a promising drug delivery system, diverse methods have been used to load them with active pharmaceutical ingredients (API) in preclinical and clinical studies. However, there is yet to be an engineered EV formulation approved for human use, a barrier driven in part by the intrinsic heterogeneity of EVs. API loading is rarely assessed in the context of single vesicle measurements of physicochemical properties but is likely administered in a heterogeneous fashion to the detriment of a consistent product. Here, we applied a suite of single-particle resolution methods to determine the loading of rhodamine 6G (R6G) surrogate cargo mimicking hydrophilic small molecule drugs across four common API loading methods: sonication, electroporation, freeze-thaw cycling and passive incubation. Loading efficiencies and alterations in the physical properties of EVs were assessed, as well as co-localization with common EV-associated tetraspanins (i.e., CD63, CD81 and CD9) for insight into EV subpopulations. Sonication had the highest loading efficiency, yet significantly decreased particle yield, while electroporation led to the greatest number of loaded API particles, albeit at a lower efficiency. Moreover, results were often inconsistent between repeated runs within a given method, demonstrating the difficulty in developing a rigorous loading method that consistently loaded EVs across their heterogeneous subpopulations. This work highlights the significance of how chosen quantification metrics can impact apparent conclusions and the importance of single-particle characterization of EV loading.

## KEYWORDS

bioengineering, drug delivery, exosomes, therapeutics

## 1 | INTRODUCTION

Extracellular vesicles (EVs) are heterogenous lipid-bilayer wrapped nanoparticles released by all cells and play a critical role in cell-to-cell communication (Buzas, 2022; Van Niel et al., 2022). EVs have great potential as next-generation drug delivery vehicles given their inherent biocompatibility and abilities to traffic therapeutic cargo across endothelial barriers to target-specific tissues and cells (Alvarez-Erviti et al., 2011; Cooper et al., 2014; Elsharkasy et al., 2020; Herrmann et al., 2021).

EVs also provide a platform for engineering and can be altered to add exogenous functional cargo supplementing their native biomolecular cargo. Both native and engineered EVs are under intense scrutiny for efficacy across many indications in preclinical and clinical studies (Castilla et al., 2021; Herrmann et al., 2021). In many of these studies, active pharmaceutical ingredients (APIs) are loaded into EVs (before or after EV isolation) using a suite of diverse methods. API loading methods can be performed

This is an open access article under the terms of the [Creative Commons Attribution-NonCommercial-NoDerivs License](https://creativecommons.org/licenses/by-nc-nd/4.0/), which permits use and distribution in any medium, provided the original work is properly cited, the use is non-commercial and no modifications or adaptations are made.

© 2024 The Author(s). *Journal of Extracellular Biology* published by Wiley Periodicals LLC on behalf of International Society for Extracellular Vesicles.

before EV isolation, such as via manipulation of the parent cells using transfection, incubation or UV irradiation (Castilla et al., 2021). Loading methods performed after EV isolation are largely divided into two groups: physical (electroporation, sonication and freeze-thaw cycling) and chemical (transfection and organic solvent) (Castilla et al., 2021). Each of these methods induces EV cargo loading via different physical means and are associated with certain strengths and weaknesses. Electroporation and sonication temporarily porate the EV membrane, allowing the API to enter the EV lumen (Gehl, 2003; Xi et al., 2021). Freeze-thaw cycling causes changes in membrane fluidity during fluctuating temperature, increasing membrane permeability without poration (Cooper et al., 2014). Chemical methods induce transient EV membrane permeability, for example, saponin molecules bind to cholesterol in the lipid bilayer of the EV membrane and form small pores. Yet the unloaded chemicals are difficult to remove after loading and typically induce cytotoxicity themselves (Xi et al., 2021).

Despite the acknowledgement of the highly heterogeneous nature of EVs (Poupardin et al., 2021; Théry et al., 2018), a glaring weakness of the prior work to load various APIs into EVs is a lack of critical comparison across techniques, resulting in no accepted 'gold standard' approach (Donoso-Quezada et al., 2020). Even within each loading method, there are few examples of rigorous optimization (Lennaárd et al., 2021). Moreover, there is rarely any consideration for the intrinsic particle-to-particle heterogeneity within a therapeutic EV preparation, which may be reflected in the particular efficiencies of each technique to load a desired API.

API loading efficiencies are generally characterized in bulk, commonly described as the ratio of the amount of API loaded to EV quantity (measured through protein quantity or count) (Lennaárd et al., 2021; Haney et al., 2015; Pomatto et al., 2019). These calculations assume that APIs are loaded equally across EVs and that the EV count measurement was made accurately, despite known challenges (Bachurski et al., 2019). This oversight is significant as many of the desired, beneficial characteristics of EVs in the context of their therapeutic application can be ascribed to specific proteins and their presence in subpopulations of EVs is likely (Jeppesen et al., 2019). Furthermore, the difference in size of EVs can affect the composition and function of EVs (Caponnetto et al., 2017; Mathieu et al., 2021). It is therefore important to assess API loading in the context of single vesicle measurements of size and composition (Chen et al., 2021; Chen et al., 2023; Silva et al., 2021), but this is rarely performed, despite known inconsistencies in engineering methods (Hood et al., 2014; Johnsen et al., 2016).

To better understand the heterogeneity of API loading in EV populations, we applied several common API loading methods using surrogate small molecule cargo to assess loading efficiency and changes in EV physicochemical properties at the single particle level.

## 1.1 | Materials and methods

### 1.1.1 | EV generation and collection

CELLine AD 1000 bioreactors were utilized for cell culture with 15 mL cell compartments and 1 L media compartment separated by a 10 kDa semi-permeable membrane. HEK 293T cells were plated and expanded to at least  $2.5 \times 10^7$  cells, the minimum concentration necessary to seed the bioreactor. During cell expansion, Dulbecco's Modified Eagle's Medium (DMEM) with 10% fetal bovine serum, 2 mM L-glutamine and 1% penicillin/streptomycin was used. Cells between passages 3 and 5 were seeded into the cell compartment of the bioreactor. The media compartment was filled with 1 L of DMEM with 2 mM L-glutamine and 1% penicillin/streptomycin. To ensure that cells were fully adherent, they were seeded in complete medium. Twenty-four hours after cell seeding, media in the cell compartment was replaced with EV-depleted media to support downstream isolation of cell-secreted EVs. To prepare EV-depleted media, DMEM with 10% fetal bovine serum, 2 mM L-glutamine and 1% penicillin/streptomycin was centrifuged overnight at  $120,000 \times g$  and then filtered. After 7 days, media in the cell compartment was collected for EV isolation and both cell and media compartment were replaced. This was repeated each week for up to 15 weeks. While the use of bioreactors differs from more traditional flask cell culture conditions, this method allows for the generation of high numbers of EVs due to the concentrated number of cells in the 15 mL cell compartment (Artuyants et al., 2021) and EVs isolated from bioreactors have previously been characterized to have consistent EV tetraspanin expression over weeks of isolation (Mizenko et al., 2021).

### 1.1.2 | EV isolation

The collected cell media from the cell compartment of the bioreactors was diluted to 30 mL with PBS and then centrifuged at  $300 \times g$  for 10 min at  $4^\circ\text{C}$  to remove cells. The supernatant was collected and centrifuged at  $2000 \times g$  for 15 min at  $4^\circ\text{C}$  to remove dead cells. The supernatant was collected and centrifuged at  $10,000 \times g$  for 30 min at  $4^\circ\text{C}$  to remove cell debris. The supernatant was collected and stored at  $-80^\circ\text{C}$ . Three consecutive weeks' worth of supernatant was ultracentrifuged at  $120,000 \times g$  for 70 min at  $4^\circ\text{C}$  in parallel to pellet EVs. Each pellet was resuspended in filtered PBS ( $0.2 \mu\text{m}$ ) and then combined for a final volume of 30 mL. The combined resuspended EV solution was again ultracentrifuged at  $120,000 \times g$  for 70 min at  $4^\circ\text{C}$ . The supernatant

was discarded, and the pellet was resuspended in 250  $\mu\text{L}$  of filtered (0.2  $\mu\text{m}$  polyether sulfone membrane filters, Corning) PBS. This solution was aliquoted into 1.5 mL Protein LoBind Eppendorf tubes to minimize free-thaw cycles and frozen at  $-80^{\circ}\text{C}$  until used. EV sample dilution, storage and handling in all downstream experiments were performed using 1.5 mL Protein LoBind Eppendorf tubes.

### 1.1.3 | Fluorescence labelling

For each loading experiment, EV stock from a single isolation were used. Each EV isolation was independently isolated and was  $\sim 1.5\text{E}12$  particles per mL in concentration by NTA. To non-specifically label EVs, stock EVs were diluted with 40  $\mu\text{M}$  carboxyfluorescein succinimidyl ester (CFSE) at a ratio of 1:14 (EV:CFSE) and incubated for 1 h at  $37^{\circ}\text{C}$ . For unlabelled control studies, EVs were diluted with filtered PBS (0.2  $\mu\text{m}$ ) at a ratio of 1:14 (EV:PBS) and were also incubated for 1 h at  $37^{\circ}\text{C}$ . For loading EVs, surrogate cargo rhodamine 6G (R6G) was used. R6G stock solution was prepared by dissolving R6G in PBS at a concentration of 7 mM and then filtering (0.2  $\mu\text{m}$ ) the solution. A total 60  $\mu\text{L}$  of the EV solution was mixed with 120  $\mu\text{L}$  of the R6G solution. For control studies with R6G only (no EVs), 120  $\mu\text{L}$  of the R6G solution was mixed with 60  $\mu\text{L}$  of filtered PBS.

### 1.1.4 | Quantitative cryo-electron microscopy (qCryoEM)

Copper grids (Quantifoil, 1.2  $\mu\text{m}$  diameter holes, 1.3  $\mu\text{m}$  separation, 300 M Cu grid) were cleaned using glow discharge for 25 s at 15 mA negative polarity (PELCO easiGlow, Ted Pella). For EV characterization, EV stock solution was used. For characterization of EVs after R6G loading, samples before size exclusion chromatography (SEC) were used to maximize EV concentration. 10  $\mu\text{L}$  of sample was placed on parafilm and the prepared copper grids were floated on the top of the drop for 30 min at room temperature. The grids were then loaded onto the Leica EM GP2 Plunge Freezer. The grid was blotted for 4 s then flash frozen. Grids were stored in liquid nitrogen until imaged. Imaging of the grids was performed on the ThermoFisher Glacios at  $11,000\times$  magnification. Images were analyzed using Adobe Photoshop 2023 (version 24.4.1) and contrast was increased for ease of visualizing the delimiting membrane. The line tool was used to measure the diameter of the imaged EVs in pixels and converted into nm. The morphology and lamellarity of each EV were also recorded. At least 100 EVs were measured for each condition.

### 1.1.5 | Nanoparticle tracking analysis (NTA)

To determine the size and concentration of EVs, EVs were diluted in filtered (0.02  $\mu\text{m}$ ) PBS and analyzed by NanoSight LM10 (Malvern Panalytical Ltd., UK). The LM10 was equipped with a 405 nm laser module, a sCMOS camera and an automated syringe pump (Harvard Bioscience, MA). The instrument tubing was cleaned with ethanol and rinsed with filtered PBS before use. The EVs were diluted to  $1\times 10^8$  to  $1.5\times 10^9$  particles per mL. Three, 30 s videos were obtained at camera levels 11–12 and data analysis was performed using NanoSight NTA 3.4 with a detection threshold 2–3.

### 1.1.6 | Resistive pulse sensing (RPS)

RPS was performed on nCS1 (Spectradyne) using C-400 cartridges (Spectradyne). Buffer solution of 1% tween-20 (BioRad) and 1x PBS (Sigma-Aldrich) filtered with 0.2  $\mu\text{m}$  non-pyrogenic filter was freshly prepared prior to each use. To prime the instrument, a reusable cleaning cartridge was run. Internal calibration standard 200 nm polystyrene bead (3000 Series Nanosphere Size Standard, ThermoFisher) solution was prepared by diluting stock bead solution by 1000 times in the buffer solution that was further filtered by a 0.02  $\mu\text{m}$  filter. EV samples were then diluted in the bead solution for a final EV concentration between  $5\times 10^9$  and  $2\times 10^{10}$  particles per mL. Three microliters of the EV and bead solution was run on the C-400 cartridge. RPSpass software (version 1.0.2.0) was then used to analyze the data and remove outliers and calibrate using the standard beads.

### 1.1.7 | Tetraspanin immunocapture assay

Leprechaun “exosome human tetraspanin” kits (Unchained Labs) were stored in  $4^{\circ}\text{C}$  and chips were warmed to room temperature before use. Chips were pre-scanned to identify any pre-existing adhered particles according to the provided protocol. For initial characterization of isolated EVs, stock EVs were diluted 1:1000 with filtered PBS (0.2  $\mu\text{m}$ ). Then 5  $\mu\text{L}$  of EV solution was diluted with 45  $\mu\text{L}$  of 1x incubation solution (provided 10x incubation solution was diluted to 1x concentration with milliQ water with 0.2% BSA). For sample incubation, chips were placed in the provided 24-well plate and 35  $\mu\text{L}$  of diluted sample was pipetted

onto the centre of the chip. The 24-well plate was then sealed, covered in aluminium foil and allowed to incubate overnight. After incubation, 300  $\mu\text{L}$  per chip of 1x blocking solution and 0.6  $\mu\text{L}$  per chip of anti-CD9, anti-CD63 and anti-CD81 antibodies were prepared. Chips were then washed with the ExoView CW1000 Plate Washer (Unchained Labs) on the CW-TETRA protocol. A total of 250  $\mu\text{L}$  per chip of prepared blocking solution was added when prompted. Chips were then transferred to the chuck and imaged using ExoView R100 Automated Imager (Unchained Labs). Data was analyzed using ExoView Analysis Software (Unchained Labs). Fluorescent cutoffs were chosen to limit the particle count on the MIgG capture spot to be less than approximately 100 particles. For R6G loading sample analysis, 5  $\mu\text{L}$  of sample from SEC were diluted with 45  $\mu\text{L}$  of 1x incubation solution (provided 10x incubation solution was diluted to 1x concentration with milliQ water with 0.2% BSA). Samples were incubated as described above. After incubation, 300  $\mu\text{L}$  per chip of 1x blocking solution and 0.6  $\mu\text{L}$  per chip of anti-CD63 antibody was prepared. Chips were then washed as described above. Data was analyzed using ExoView Analysis Software (Unchained Labs). The same cutoffs were used on all chips: 300 AU, 250 AU and 450 AU (AU stands for arbitrary units) for the red, green and blue channel, respectively. These fluorescent cutoffs were chosen to limit the particle count on the MIgG capture spot to be approximately less than 100 events with control samples with only free R6G dye. Additionally, EV concentration on chips were maintained within the single-particle range (Figure S1) (Mizenko et al., 2021). Despite this precaution, there is a non-zero chance that a single detected particle on the tetraspanin immunocapture assay could represent more than one EV. Each point shown on graphs for loading efficiency and detected particle numbers are the average of three capture spots (one each of CD63, CD81 and CD9).

### 1.1.8 | Sonication

Probe sonicator (Sonics & Materials, Ultrasonic Processor VCX 130) was used to sonicate samples at 130 W, 120 kHz and 30% amplitude unless otherwise noted. Samples were sonicated for 3 or 6 treatment cycles. One treatment cycle was 30 s of sonication (with or without pulsing of 4 s on and 2 s off) and 3 min of rest at 19°C.

### 1.1.9 | Electroporation

Samples were incubated at 19°C for 30 min and then transferred to 0.4 cm electroporation cuvettes (Bio Rad). Samples were electroporated with a single exponential decay wave at 125  $\mu\text{F}$  and various voltages (BioRad, Gene Pulser Xcell Total System). Samples were transferred into Eppendorf tubes using disposable polyethylene transfer pipets (Fisher Scientific) and immediately stored on ice.

### 1.1.10 | Freeze-Thaw

Samples were incubated at 19°C for 30 min. Samples were then subjected to various numbers of freeze-thaw cycles. One freeze-thaw cycle was 5 min at  $-80^\circ\text{C}$  and 10 min at 19°C.

### 1.1.11 | Size exclusion chromatography (SEC)

After the various loading methods were conducted, SEC was performed to isolate EVs from unloaded R6G and free dye. SEC was conducted with Automatic Fraction Collectors (AFC) V2 and qEVsingle/35 Gen2 (Izon) to isolate EVs from the free dye. AFC V2 Firmware Version 1.2.2 was used. One collection of 0.8 mL and default buffer volume (0.87 mL) was used. Following the provided protocol, each column was flushed with 6 mL of 0.2  $\mu\text{m}$  filtered PBS. Once done flushing, the remaining PBS was removed and 150  $\mu\text{L}$  of sample was added. Once the sample had passed through the frit, at least 2 mL of filtered PBS was added. Isolated EV samples were used the same day for downstream analysis with tetraspanin immunocapture, NTA and/or RPS.

### 1.1.12 | Statistical methods

Error bars represent one standard deviation from the mean. Statistical significance was assessed by comparing three or more populations using ANOVA and conducted with MATLAB (R2023a Update 2). Bars with no common letters are significantly different ( $p < 0.05$ ).

Outliers for R6G intensity and qCryoEM data were determined using GraphPad Prism using the ROUT methods with a coefficient Q of 1% (version 10.1.0). For morphological CryoEM data, a Chi-squared test of independence was performed to

**TABLE 1** Summary of the single-particle EV characterization methods, including the mode of readout and limit of detection in this work.

Measurement	Readout	Limit of detection
NTA	Particle size distribution and concentration based on light scattering	80 nm
RPS	Particle size distribution and concentration based on changes in electrical resistance	65 nm
qCryoEM	EV size distribution and morphology	<1 nm
Tetraspanin assay—immunofluorescence	Particle number and intensity based on fluorescence of capture spot (i.e., CD63, CD81 and CD9)	Fluorescence detection thresholds set based on control MIgG
Tetraspanin assay—interferometry (SP-IRIS)	Particle size distribution based on interference of two reflected light paths and categorized by capture spot (i.e., CD63, CD81 and CD9)	Size detection threshold set to be between 50 to 200 nm (assuming EV refractive index, $n = 1.4$ )

determine if there was a significant association between the treatment conditions and the categories of EVs. Post-hoc analysis involved calculating standardized residuals to identify significant deviations between observed and expected frequencies.

## 2 | RESULTS

In this study, we applied a suite of single-particle characterization methods to determine the loading of surrogate cargo across four common API loading methods: sonication, electroporation, freeze-thaw cycling and simple mixing (passive incubation) (Castilla et al., 2021). Rhodamine 6G (R6G) was used as a small, membrane impermeant, hydrophilic surrogate cargo, chosen due to its fluorescence character, which was used to track loading across single EVs. While analytical tools with single particle resolution are used, most results were reported as population averages.

### 2.1 | Single EV characterization prior to loading

HEK293T cell EVs were isolated from the conditioned media of a bioreactor using ultracentrifugation (UC). We devised a comprehensive EV characterization strategy focused on orthogonal methods with single particle resolution and in compliance with MISEV guidelines, summarized in Table 1 (Théry et al., 2018; Welsh et al., 2024). Overall, we sought to assess loading efficiencies, changes in physical properties and co-localization with common EV-associated tetraspanins (i.e., CD63, CD81 and CD9) as a proxy to examine distribution across EV subpopulations.

To orthogonally assess particle size and number concentration of EVs prior to loading, we performed quantitative cryo-electron microscopy (qCryoEM), nanoparticle tracking analysis (NTA) and resistive pulse sensing (RPS), while hybrid interferometry/immunofluorescence imaging (SP-IRIS, ExoView R100 Automated Imager) was performed to size and examine composition of chip-captured EVs (Figure 1). qCryoEM images (Figure 1a) of the isolated particles were quantified, revealing that most particles appeared to be EV-like, with unilamellar, circular morphology and mean diameter under 100 nm (Figure 1b). Approximately 30% of the particles were multilamellar and/or non-circular in shape, and these EVs (especially the non-circular ones) were more likely to be larger in diameter. Orthogonal methods of NTA, RPS and interferometry also produced size distributions of the isolated EVs (Figure 1c). RPS, qCryoEM and interferometry yielded mean sizes of 74.7, 68.3 and 97.4 nm, respectively, and each displayed a log-linear relationship between particle count and size. Interestingly, a bimodal size distribution can be observed in the qCryoEM size distribution, with the second peak around 150 nm in diameter. Instead, NTA measured a mean size of 123.4 nm with a more Gaussian-shaped curve, presumably due to its inefficiency to detect smaller biological nanoparticles with low scattering efficiency and higher sensitivity to larger, highly scattering particles (Bachurski et al., 2019). Particle concentration was measured by NTA to be  $5.3 \times 10^{12}$  particles/mL and by RPS to be  $2.63 \times 10^{12}$  particles/mL, in relative concert with one another (and modern reports on EV characterization) despite the different sensitivities to size. The total protein in the EV isolation was also determined and was measured to be 1.55E10 particles per  $\mu\text{g}$  protein, which corresponds to minimal protein contamination in the isolation (Webber & Clayton, 2013).

The presence and colocalization of EV biomarkers CD9, CD63 and CD81 was confirmed with immunocapture (Figures 1d and S2). Tetraspanin-based EV capture was carried out using antibody microarrays, with each spot decorated with capture antibodies against either CD81, CD63, CD9 or mouse immunoglobulin G (MIgG) as a non-specific binding control (Figure 1e). After EV incubation with the microarrayed chip, additional fluorescent detection antibodies against CD81, CD63 or CD9 were added. For downstream experiments to assess R6G loading the three fluorescent channels were used to detect (1) carboxyfluorescein

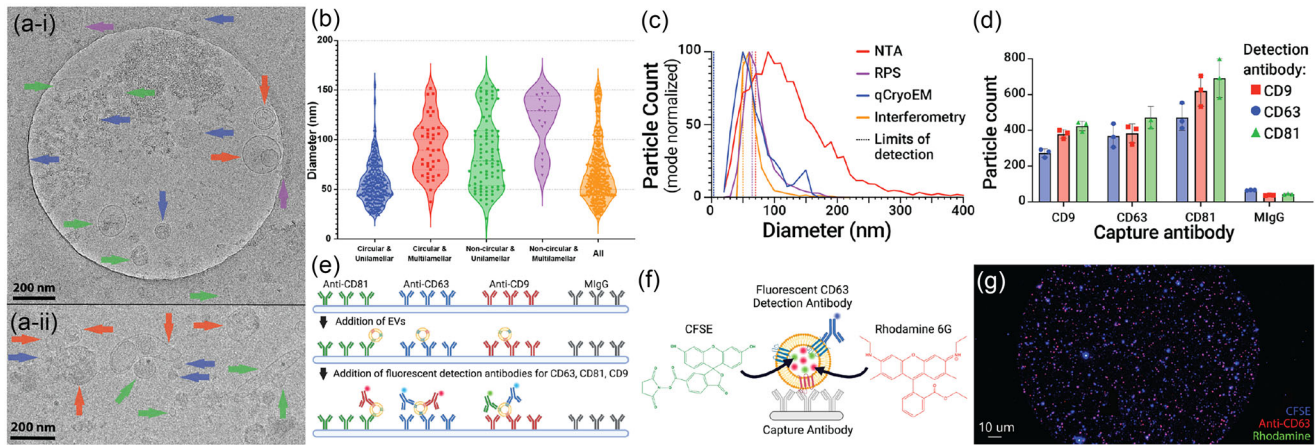


**FIGURE 1** Characterization HEK293T EVs prior to loading. (a) Representative qCryoEM images of isolated particles, with arrows indicating vesicles and (b) the corresponding quantification of size distribution categorized by EV morphology and lamellarity ( $n = 433$ ). Blue, red, green and purple arrows indicate C&UL, C&ML, NC&UL and NC&ML EVs, respectively. (c) Orthogonal size distributions from NTA (red), RPS (purple), qCryoEM (blue) and hybrid interferometry/immunofluorescence imaging (orange), with corresponding limits of detection for each technique indicated by vertical dashed lines of the respective colour. (d) An immunofluorescence assay was used to assess the presence and colocalization of common EV tetraspanins CD9, CD63 and CD81, alongside non-specific control MIgG. (e) Schematic showing workflow for the immunofluorescence assay. (f) Schematic showing labelling strategy for assessing loading with EV specific anti-CD63, CFSE as a non-specific EV label, and R6G as the surrogate loaded cargo. (g) Microarray fluorescence image showing a single spot decorated with captured EVs (blue channel: CFSE, red channel: CF647-anti-CD63, green channel: R6G). Figure 1e,f were created with BioRender. C, circular; ML, multilamellar; NC, non-circular; UL, unilamellar.

succinimidyl ester (CFSE), a non-specific EV dye, (2) the loaded R6G cargo and (3) anti-CD63 CF647 antibody and the resulting chip was imaged (Figure 1f,g). The MIgG capture spot was used to set fluorescent detection thresholds for each channel.

## 2.2 | Sonication loading

For sonication-based loading, EVs incubated with R6G were probe sonicated for one ‘treatment cycle,’ which was defined as 30 s followed by 3 min of rest at room temperature for various number of cycles. Pulsing was also tested during the sonication period (i.e., 4 s on/ 2 s off). The specific duration for each cycle and pulse rate were chosen based on prior literature for EV drug loading (Haney et al., 2015; Lamichhane et al., 2016; Rajendran et al., 2021). Incubation of EVs with R6G without sonication was used as the negative control to which comparisons were made to account for passive loading and electrostatic interactions due to their opposing charges (anionic EVs vs. cationic R6G). After EVs were loaded, SEC was then used to isolate EVs from free CFSE and R6G.

The number of detected particles by immunofluorescence readout from the tetraspanin assay was used to determine EV loading efficiency, defined as the ratio of detected R6G<sup>+</sup> particles to either the number of detected CFSE<sup>+</sup> particles, CD63<sup>+</sup> particles (i.e., detected fluorescent anti-CD63 antibodies), or total particle number (Figure 2a). Three different parameters were used to calculate loading efficiency given the limitation of each. CD63<sup>+</sup> EVs represent a subpopulation given that not all EVs express CD63. While CFSE is non-specific EV label, there is no guarantee that CFSE labelling is homogenous. Furthermore, there may have been CFSE labelled EVs below the limit of detection for that fluorescent channel. Finally, total particle number was used as a more potentially more holistic parameter, but this still represents tetraspanin enriched EVs. Despite these limitations, regardless of which of these three populations was used, loading efficiencies were significantly greater than via passive loading with no significant differences across sonication conditions (3 or 6 cycles, with or without pulsing). Notably, examination of the raw number of R6G<sup>+</sup>, CFSE<sup>+</sup> or CD63<sup>+</sup> particles reveals that the number of CFSE<sup>+</sup> and CD63<sup>+</sup> particles decreased with increased sonication treatment cycle number while R6G<sup>+</sup> particles remained largely unchanged or even slightly decreased (Figure 2b). Pulsing resulted in preservation of more particles within each group of the same number of cycles. Taken together, while bulk loading efficiencies suggest sonication increases R6G loading compared to passive incubation, single EV analysis reveals how sonication may negatively affect EV integrity and lead to fusion or degradation of EVs.

Next, we considered differential loading across CD63<sup>+</sup>, CD81<sup>+</sup> and CD9<sup>+</sup> EV subpopulations isolated by capture spot on the tetraspanin kit assay. R6G<sup>+</sup> particle count for each tetraspanin-enriched subpopulation was normalized by total particle count (Figure 2c). There was a significant increase in the relative amount of R6G-loaded into CD81<sup>+</sup> and CD9<sup>+</sup> EVs, but not CD63<sup>+</sup> EVs, suggesting that R6G loading via sonication is heterogenous and preferential into CD81<sup>+</sup>/CD9<sup>+</sup> subpopulations of EVs.

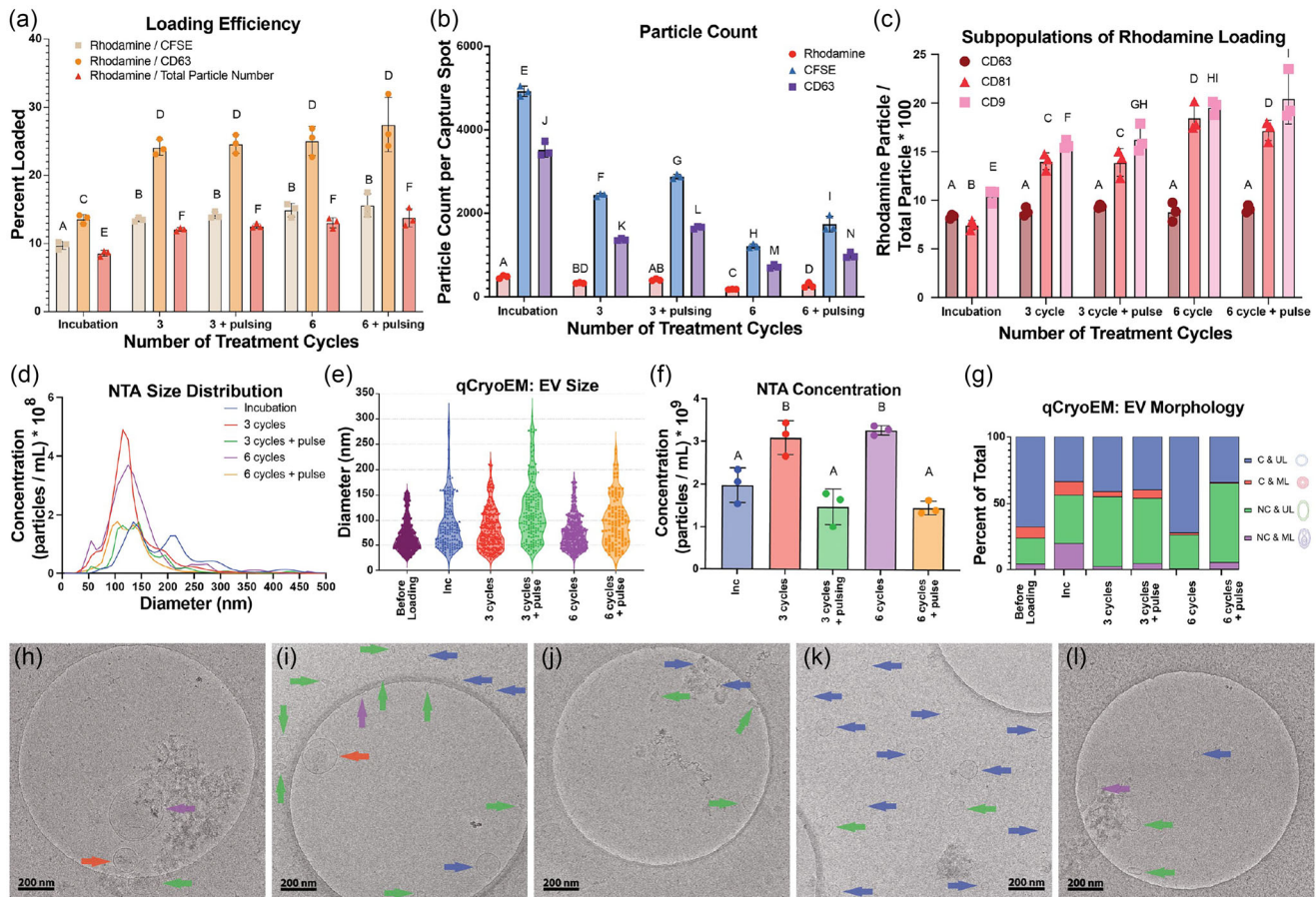


**FIGURE 2** Loading EVs with R6G via sonication using various cycle numbers with and without pulsing. One cycle consisted of 30 s of sonication with or without pulsing (4 s on/ 2 s off) and 3 min of rest at room temperature. R6G loading into EVs was characterized by using the immunofluorescence readout of tetraspanin capture assays and quantified as (a) loading efficiency, defined as ratio of R6G-loaded EVs to total EV count (using either the number of detected CFSE particles, CD63<sup>+</sup> particles or total particle number), (b) particle count and (c) subpopulations of R6G-loaded EVs. (d) NTA and (e) qCryoEM were used size distribution of samples after loading. (f) NTA was used to determine concentration of samples after loading. (g) qCryoEM was used to determine morphology after loading. Representative CryoEM images with arrows pointing to EVs from (h) the incubation sample, and samples sonicated for (i) 3 cycles, (j) 3 cycles with pulse, (k) 6 cycles and (l) 6 cycles with pulse. Blue, red, green and purple arrows indicating C&UL, C&ML, NC&UL and NC&ML EVs, respectively. C, circular; Inc, incubation; ML, multilamellar; NC, non-circular; UL, unilamellar. Bars with no common letters are significantly different (ANOVA,  $p < 0.05$ ).

The size of R6G-loaded EVs by interferometry showed a decrease in EVs between 100 and 200 nm following R6G loading, suggesting that sonication preferentially loaded smaller EVs, caused a decrease in EV size, and/or caused fusion of EVs putting them out of the upper range of detection by interferometry (<200 nm) (Figure S3a–e). Supporting this interpretation, the fluorescence intensity of R6G<sup>+</sup> particles across all capture antibodies revealed that the majority of the detected particles were not within the interferometry measurements cutoffs (between 250 and 500 AU in intensity representing >75% of the captured particles), which means the particles were either smaller than 50 nm or larger than 200 nm (Figure S3f–j). NTA and qCryoEM analyses suggest that the majority of particles were indeed smaller than 200 nm regardless of loading method. NTA measured a mean diameter of 194.6, 142.5, 151.6, 136.8 and 129.1 nm for the samples loaded via incubation, three cycles, three cycles with pulsing, six cycles, and six cycles with pulsing, respectively (Figure 2d). qCryoEM revealing the presence of EVs smaller than 50 nm (Figure 2e). Taken together, these data suggest that most R6G-loaded EVs are the smaller, sub-50 nm EVs.

Particle concentration by NTA increased after sonication, but only without pulsing (Figure 2f). This is unexpected given that CFSE<sup>+</sup> and CD63<sup>+</sup> particle count decreased with sonication cycles (Figure 2b) but could be explained by considering the detection limitations of NTA, which may be unable to detect smaller particles.

With respect to EV morphology (by qCryoEM), passive incubation promoted the formation of non-circular and multilamellar EVs that were not found after sonication (Figures 2g–l and S4). This change in morphology was found to be a significant deviation with a Chi-squared residual of 5.7. Additionally, six sonication cycles without pulsing promoted the formation of unilamellar, circular EVs (Figure 2k). All observed changes in morphology were found to be statically significant (Chi-squared,  $p = 2.92E-18$ ).



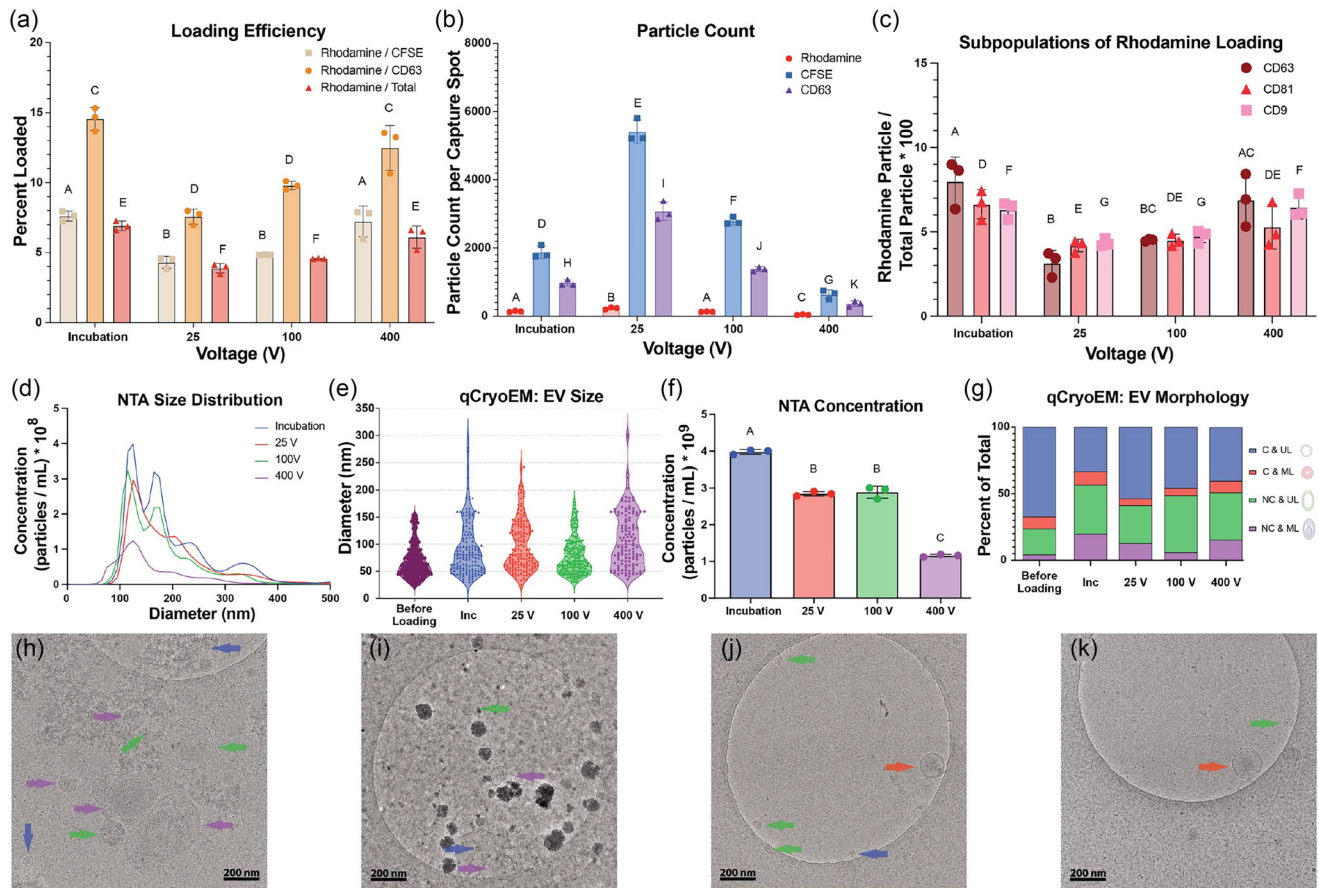


**FIGURE 3** Loading of EVs with R6G via electroporation. EVs were electroporated with a single pulse at various voltages and 125  $\mu$ F. The loading of R6G into the EVs was characterized by using the immunofluorescent readout of tetraspanin immunocapture assays and quantified as (a) loading efficiency, (b) particle count, and (c) subpopulations of R6G-loaded EVs. (a) Loading efficiency was defined as ratio of R6G-loaded EVs count (number of detected R6G particles) to total EV count (number of detected CFSE particles, CD63 particles, or total particle number). (d) NTA and (e) qCryoEM were used size distribution of samples after loading. (f) NTA was used to determine concentration of samples after loading. (g) qCryoEM was used to determine morphology after loading. Representative CryoEM images with arrows pointing to EVs from (h) the incubation sample, and samples after electroporation at (i) 25 V, (j) 100 V and (k) 400 V. Blue, red, green and purple arrows indicating C&UL, C&ML, NC&UL and NC&ML EVs, respectively. C, circular; Inc, incubation; ML, multilamellar; NC, non-circular; UL, unilamellar. Bars with no common letters are significantly different (ANOVA,  $p < 0.05$ ).

### 2.3 | Electroporation loading

Next, electroporation-based loading of R6G was examined using 125  $\mu$ F and either 25, 100 or 400 V, chosen around values typically found in the literature (Alvarez-Erviti et al., 2011; Chen et al., 2023; Johnsen et al., 2016; Kooijmans et al., 2013; Kamerkar et al., 2017; Lamichhane et al., 2015; Lamichhane et al., 2016). Again, passive incubation of EVs with R6G was used as the negative control to which comparisons were made. Following electroporation at 25 and 100 V, there was an apparent decrease in loading efficiency, yet no discernable difference at 400 V from passive incubation (Figure 3a). However, the number of R6G<sup>+</sup> particles only increased with 25 V and decreased with 400 V (Figure 3b). Furthermore, the number of CD63<sup>+</sup> and CFSE<sup>+</sup> particles were observed to increase at 25 and 100 V, which may be due to the splitting of EVs into smaller EVs during the electroporation process. Contrary to sonication, CFSE<sup>+</sup> and CD63<sup>+</sup> particles increased dramatically at 25 and 100 V, but decreased at 400 V (Figure 3b). Subpopulations of R6G-loaded EVs were again investigated by tetraspanin capture following electroporation (Figure 3c). Within the R6G<sup>+</sup> EVs, the number of CD63<sup>+</sup>, CD81<sup>+</sup> and CD9<sup>+</sup> EVs initially dropped at 25 V but then increased with increased voltage.

To further characterize the R6G-loaded EVs, their size was determined using interferometry (Figure S5a–d). Unlike with sonication, the number of R6G-loaded EVs between 80 and 150 nm in size increased with electroporation of 25 V and 100 V compared to incubation. Furthermore, the majority of the detected rhodamine fluorescent particles were within the interferometry threshold for the samples electroporated at 25 and 100 V (Figure S5e–h). This demonstrates the interferometry was able to depict the size distribution for majority of the R6G loaded EVs. This result is supported by NTA and qCryoEM analyses which suggest that the majority of particles are less than 200 nm in size (Figure 3d,e). Incubation, 25, 100 and 400 V samples were measured to have a mean diameter of 194.5, 192.9, 175.2 and 158.9 nm by NTA, respectively.

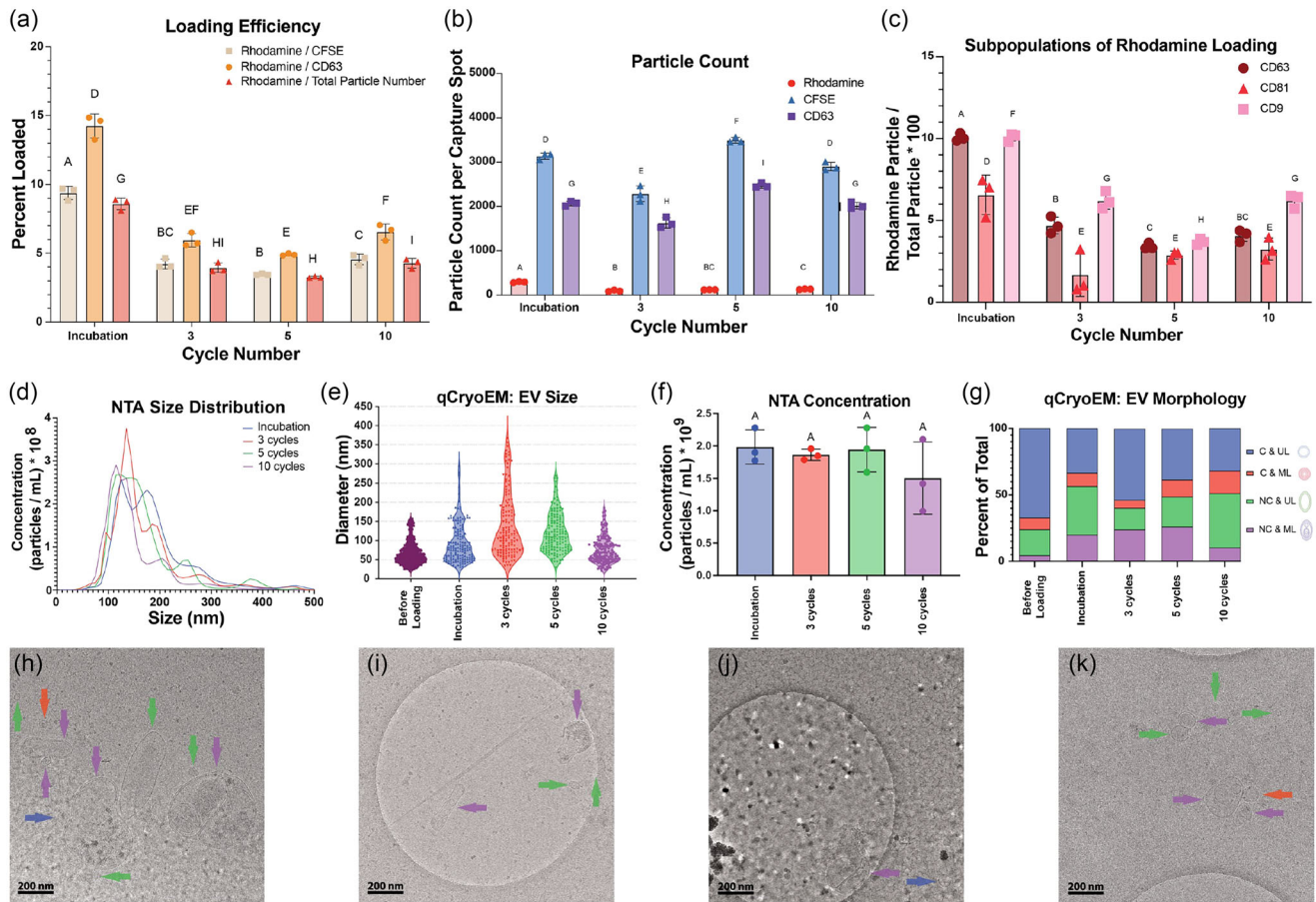


**FIGURE 4** Loading of EVs with R6G via various number of freeze-thaw cycles. Freeze-thaw cycles consisted of 5 min at  $-80^{\circ}\text{C}$  and 10 min at room temperature. The loading of R6G into the EVs was characterized by using the immunofluorescent readout of tetraspanin immunocapture assays and quantified as (a) loading efficiency, (b) particle count, and (c) subpopulations of R6G-loaded EVs. (a) Loading efficiency was defined as ratio of R6G-loaded EVs count (number of detected R6G particles) to total EV count (number of detected CFSE particles, CD63 particles, or total particle number). (d) NTA and (e) qCryoEM were used size distribution of samples after loading. (f) NTA was used to determine concentration of samples after loading. (g) qCryoEM was used to determine morphology after loading. Representative CryoEM images with arrows pointing to EVs from (h) the incubation sample, and samples after (i) 3 cycles, (j) 5 cycles and (k) 10 cycles of freeze-thaw. Blue, red, green and purple arrows indicating C&UL, C&ML, NC&UL and NC&ML EVs, respectively. C, circular; ML, multilamellar; NC, non-circular; UL, unilamellar. Bars with no common letters are significantly different (ANOVA,  $p < 0.05$ ).

Given that the particle number for non-R6G<sup>+</sup> EVs labelled with both CFSE<sup>+</sup> (internal EV marker) and CD63<sup>+</sup> (membrane marker) decreased, we initially hypothesized that EVs are largely destroyed during electroporation (Figure 3b). NTA sizing supported that conclusion, showing a decrease in concentration at all tested voltages (Figure 3f). This is contrary to the observed increase in CFSE<sup>+</sup> and CD63<sup>+</sup> particles at 25 and 100 V identified via immunocapture (Figure 3b). qCryoEM of the 400 V samples demonstrates the presence of intact EVs within detectable size range of interferometry (Figure 3e), so these incongruous findings likely cannot be explained by considering the instrument sensitivity as was the case with sonication. Finally, the morphology of EVs was also altered, with electroporation leading to increased relative numbers of multilamellar EVs, as well as a decrease in the relative number of unilamellar and circular EVs compared to EVs before loading (Figures 3g-k and S6). All observed changes in morphology were found to be statically significant (Chi-squared,  $p = 6.23\text{e-}08$ ). The more electron dense particles observed in Figure 3i are thought to be artefacts from the vitrification process of CryoEM.

## 2.4 | Freeze-thaw loading

Finally, EVs incubated with R6G were subjected to various number of freeze-thaw cycles, with each cycle consisting of 5 min at  $-80^{\circ}\text{C}$  and 10 min at room temperature. All variations resulted in significantly lower loading efficiencies compared to passive incubation samples (Figure 4a). The number of R6G<sup>+</sup> particles was significantly diminished, while the number of CFSE<sup>+</sup> and CD63<sup>+</sup> particles was largely unchanged (Figure 4b). The relative numbers of CD63<sup>+</sup>, CD81<sup>+</sup> or CD9<sup>+</sup> particles within the

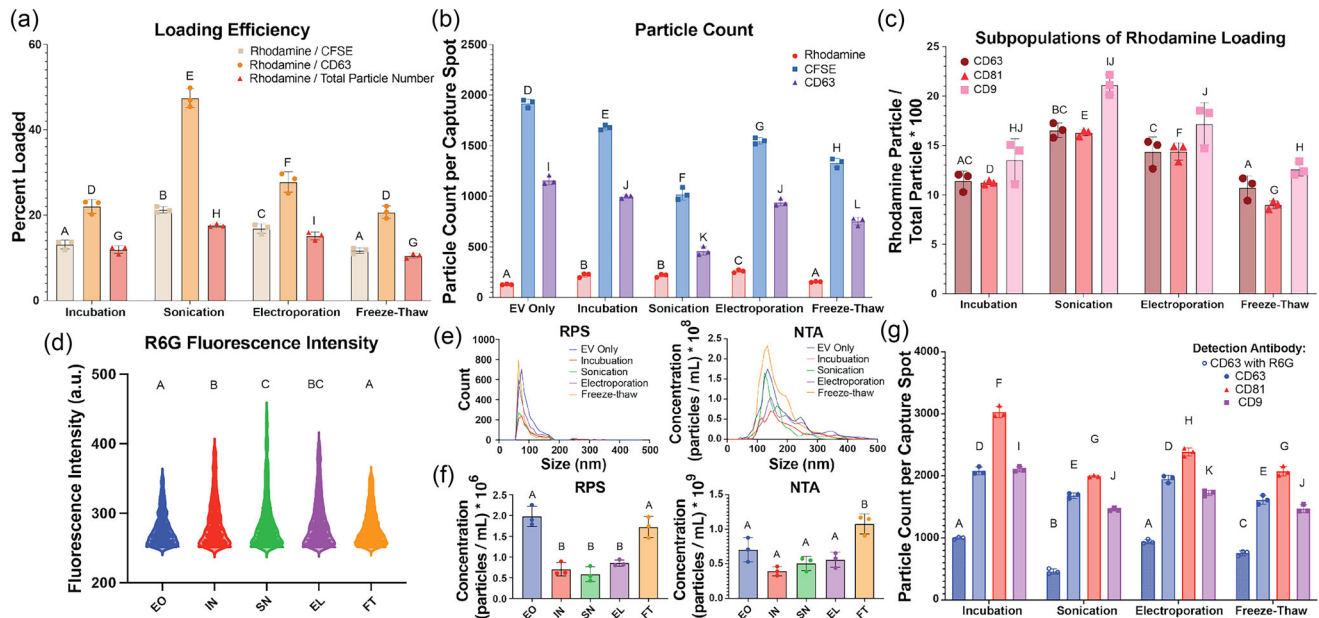


**FIGURE 5** Comparison of incubation, sonication, electroporation, and freeze-thaw to load EVs with R6G. The loading of R6G into the EVs was characterized by using the immunofluorescent readout of tetraspanin immunocapture assays and quantified as (a) loading efficiency, (b) particle count and (c) subpopulations of R6G-loaded EVs. (a) Loading efficiency was defined as ratio of R6G-loaded EVs count (number of detected R6G particles) to total EV count (number of detected CFSE particles, CD63 particles, or total particle number). RPS and NTA were used to determine (d) the size distribution and (e) concentration of samples. (f) The immunofluorescent readout of tetraspanin immunocapture assays was used to determine tetraspanin expression of unlabelled EVs incubated in PBS rather than R6G solution before and after loading methods. This was compared to the number of detected CD63 particles in the presence of R6G. Bars with no common letters are significantly different (ANOVA,  $p < 0.05$ ).

R6G-loaded EVs following freeze-thawing decreased compared to incubation (Figure 4c). Regardless of number of freeze-thaw cycles, the relative number of R6G-loaded EVs was lowest for CD81<sup>+</sup> EVs.

The number of R6G-loaded EVs between 50 and 200 nm in size decreased by interferometry, with the majority between 50–100 nm in size (Figure S7a–d). As with sonication, fluorescence intensity data shows that the majority of the detected R6G particles were not within the interferometry thresholds, signifying that they were either smaller than 50 nm or larger than 200 nm in size (Figure S7e–h). Orthogonal size measurements via NTA and qCryoEM demonstrate that the majority of the EVs were smaller than 200 nm in size. NTA measured a mean diameter of 183.3, 168.2, 166.6 and 146.2 nm for samples loaded by incubation, 3 cycles, 5 cycles and 10 cycles of freeze-thaw, respectively (Figure 4d). Furthermore, the mode size of EVs as determined by qCryoEM was smaller than 100 nm for all loading methods (Figure 4e). Together this suggests that most of the R6G-loaded EVs not captured by interferometry data were smaller than 50 nm in size. NTA results also demonstrate that the concentration of EVs was not significantly affected by freeze-thaw cycles, which supports results on detected CFSE<sup>+</sup> and CD63<sup>+</sup> particle numbers (Figure 4b,f). Lastly, freeze-thaw caused an increase in the percentage of non-circular EVs compared to EVs before loading (Figures 4g–k and S8). All observed changes in morphology were found to be statically significant (Chi-squared,  $p = 1.16e-13$ ).

## 2.5 | Comparison between methods

The individual parameters across each of the three loading methods that led to the highest number of R6G particles were used for direct comparison, that is, three treatment cycles of sonication with pulse, 25 V of electroporation, and five freeze-thaw cycles. These were also compared to passive incubation, as well as an EV-only control (i.e., CFSE-labelled EVs incubated with PBS rather than R6G). Loading efficiency was greatest for sonicated samples, followed by electroporation samples (Figure 5a). Overall, R6G-loaded particles were discernable above the autofluorescence background of the EV only control (Figures 5b and S9). The number of R6G particles was not different between EV only and freeze-thaw samples, reaffirming that freeze-thaw may not be an effective loading method for R6G or similar cargo. The greatest number of R6G particles were detected in the electroporation sample, followed by the incubation and sonication samples. The number of detected CFSE<sup>+</sup> and CD63<sup>+</sup> particles was greatest in the EV only sample, indicating that all active loading methods resulted in the loss of EVs. When looking at subpopulations within the R6G-loaded EVs, the average percent of loaded CD9<sup>+</sup> EVs was greater than CD63<sup>+</sup> and CD81<sup>+</sup> EVs for all loading methods (Figure 5c). Furthermore, percent of R6G-loaded CD63<sup>+</sup>, CD81<sup>+</sup> and CD9<sup>+</sup> EVs were significantly higher for the sonicated samples compared to the incubation sample. EV-to-EV heterogeneity in R6G intensity was also analyzed and the fluorescent

intensity of the detected R6G particles was highest in the sonicated samples (Figure 5d). Additionally, while most of the detected R6G particles are between 250 and 300 a.u., there is a large distribution of R6G fluorescent intensity (250 up to 445 a.u.).

The R6G-loaded EVs were further characterized by size using interferometry (Figure S10a–e). A majority of the R6G-loaded EVs within interferometry thresholds were between 50 and 100 nm in size. To complement this data, the fluorescence intensity data was analyzed (Figure S10f–j). For the incubation, electroporation and freeze-thaw samples, a similar number of the CD63<sup>+</sup> R6G-loaded EVs were included and excluded from the interferometry data. However, for R6G-loaded CD81<sup>+</sup> and CD9<sup>+</sup> EVs and for all sonicated EVs, a majority of the R6G detected fluorescence was excluded from the interferometry data (i.e., less than 50 nm or greater than 200 nm in size). RPS and NTA size distribution data show that the mode was between 65–75 and 120–160 nm for all samples, respectively (Figure 5e). As the limit of detection for NTA is ~70–80 nm and previously shown qCryoEM data for each loading method demonstrated a mode size around 50 nm, it is likely that most of the R6G-loaded EVs not included in the interferometry size distribution data are smaller than 50 nm in size. The RPS concentration data show a decrease in the concentration of particles in comparison to the EV only sample, except for the freeze-thaw sample (Figure 5f). On the other hand, the NTA results also show that the concentration of loaded samples does not change significantly from the EV only control, except for the freeze-thaw sample that showed no significant change in Figure 4f.

Finally, to determine the effect that the API can have on the EVs during the loading method, unlabelled EVs incubated with PBS rather than the R6G solution were subjected to the same loading methods. EVs were then characterized using immunocapture. Fluorescent anti-CD63, anti-CD81 and anti-CD9 detection antibodies were used to interrogate the samples, and this was compared to the number of detected fluorescent anti-CD63 particles in samples with R6G (Figure 5g). Interestingly, the number of detected CD63<sup>+</sup> particles without R6G were found to be around double of the number of detected particles with R6G for all loading methods. Sonication and freeze-thawing led to a decrease in the number of detected tetraspanin particles with and without R6G present compared to the incubation sample. Electroporation of the EVs did not change the number of detected CD63<sup>+</sup> particles with or without the presence of R6G compared to the incubation sample. However, the number of detected CD81<sup>+</sup> and CD9<sup>+</sup> particles decreased compared to the incubation sample. These different trends show how the various loading methods and API can affect each membrane protein differently.

## 2.6 | Comparison of incubation replicates

A limitation of this study was that it did not focus on the development or optimization of a robust loading method. Additionally, in previously shown results, each experiment used a different single EV isolation batch that was split and tested. As a result, there were differences in what subpopulations were loaded between repeated runs using EVs from different isolation batches. For instance, there were observed inconsistencies between the four incubation samples shown here that were run alongside sonication samples (run #1), electroporation samples (run #2), freeze-thaw samples (run #3) and during the method comparison (run #4). As such, here we have directly compared the incubation samples to look at the difference in these biological replicates (Figure 6). Statically significant differences were found between incubation replicates in loading efficiency (Figure 6a). Furthermore, differences in loaded subpopulations were found between incubation replicates (Figure 6b). The CD9<sup>+</sup> subpopulation had the highest average relative number of R6G-loaded EVs as determined with immunocapture in run #1 and #4, but CD63<sup>+</sup> subpopulation had the highest average in run #2 and the CD63<sup>+</sup> and CD9<sup>+</sup> subpopulation had similar averages in run #3. EV-to-EV heterogeneity in R6G fluorescence intensity was also analyzed and the distribution of fluorescent intensity of the detected R6G was fairly similar between run #1, #2 and #4 (Figure 6c). However, there was a smaller range of fluorescent intensity was observed on run #3. The size of the R6G-loaded EVs determined by interferometry was also inconsistent between runs (Figure 6d–g). The R6G-loaded EVs in runs #1, 3 and 4 were found to be mainly between 50 and 100 nm in size. However, R6G-loaded EVs were found to mainly be between 80 and 130 nm in size in run #2. This could suggest that the observed difference in size of R6G-loaded EVs according to loading method may not be due to loading method, but rather small differences in handling during loading or slight differences in cell culture conditions. For instance, experiments performed here utilized EV isolation from multiple different bioreactors and different isolation weeks (up to week 15). It has previously been shown that total particle count and protein concentration can vary between different isolation from CELLline bioreactors (Hisey et al., 2022). Additionally, there are can be differences in cell viability and shedding between bioreactors with the same cell line due differences in initial seeding density and differences environmental factors that affect growth rates.

## 3 | DISCUSSION

This study employs a suite of orthogonal techniques to evaluate API loading, including platforms based on multiple complementary modes of EV detection, such as light scattering, resistive pulse sensing and electron microscopy (cryoEM). In particular, cryoEM adds value for direction imaging of the structure of EVs (e.g., lipid bilayer) and superior preservation of EV shape (size, shape and lamellarity) compared to fixed samples. As such, cryoEM has been used to quantify size distribution and shape

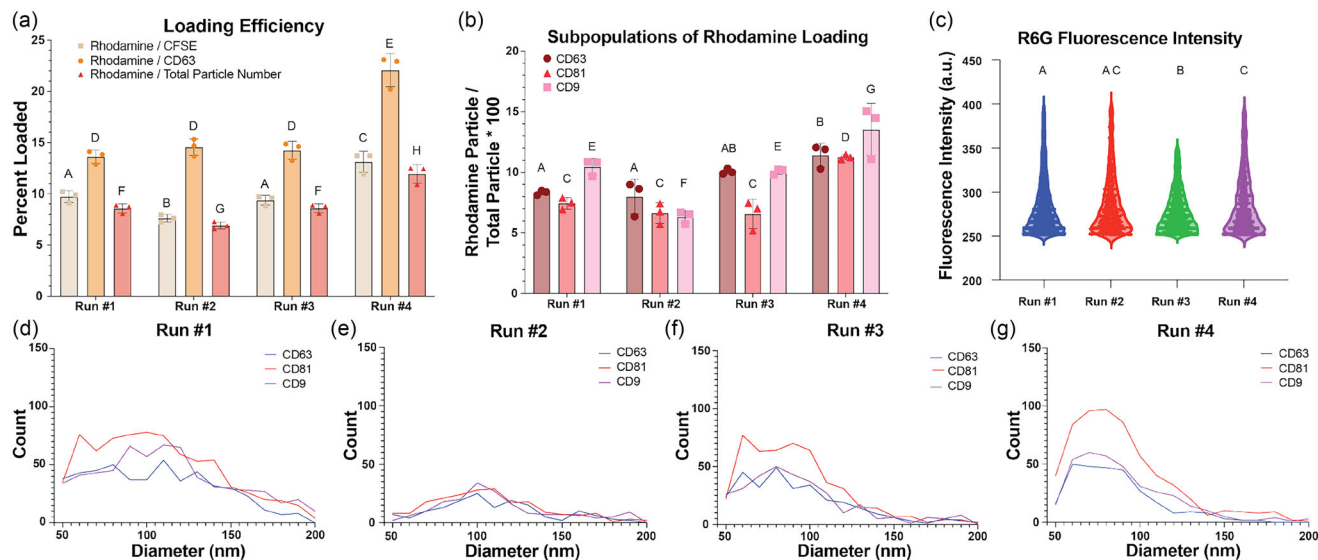


**FIGURE 6** Comparison of incubation replicates to load EVs with R6G. Incubation samples were run alongside sonication samples (run #1), electroporation samples (run #2), freeze-thaw samples (run #3) and during the method comparison (run #4). The loading of R6G into the EVs was characterized by using the immunofluorescent readout of tetraspanin immunocapture and quantified as (a) loading efficiency and subpopulations of R6G-loaded EVs. (a) Loading efficiency was defined as ratio of R6G-loaded EVs count (number of detected R6G particles) to total EV count (number of detected CFSE particles, CD63 particles, or total particle number). (d) Tetraspanin immunocapture was also used to determine the size distribution of R6G-loaded EVs via interferometry. Bars with no common letters are significantly different (ANOVA,  $p < 0.05$ ).

of native EVs. More commonly, cryoEM is used as part of MISEV guidelines for the characterization of isolated EVs. Despite its clear advantages, cryoEM is not commonly used, due to its expense, laborious nature and preanalytical variance, as well as the needs for specialized technicians and highly concentrated samples. CryoEM quantification of size, shape and lamellarity of engineered EVs is a major strength of this study, and has revealed key differences in loading across the methods tested.

In particular, we found that sonication led to a significantly greater percent EVs loaded compared to passive incubation, but on closer evaluation using orthogonal single particle characterization to analyze population averages, this trend was found to be due to a decrease in the number of total detected particles used for normalization (Figure 2a,b). This is at odds with previously published results showing that the EV encapsulation ratio (percent drug loaded EVs to total EVs) for doxorubicin was lower for sonicated samples compared to incubated samples (Chen et al., 2023). This could be due to differences in cargo properties (hydrophobic doxorubicin) or sonication type (probe vs. water bath) and time.

We also found that electroporation led to a significant decrease in CD63<sup>+</sup> particle count and overall EV concentration (Figure 3b,f), a finding comparable to results of electroporation reported in the literature resulting in poor EV recovery (defined as the ratio of output to input as measured by NTA) between ~10% and 20% (Lennaárd et al., 2021). Using a similar metric, we measured ~30% EV recovery here. Other studies did not report any EV damage or decrease in EV concentration, yet largely did not employ orthogonal single particle characterization methods (Alvarez-Erviti et al., 2011; Chen et al., 2023; Johnsen et al., 2016; Kooijmans et al., 2013; Kamerkar et al., 2017; Lamichhane et al., 2015, 2016). An additional influence on the disparate findings may be due to differences in electroporation buffer, which has been shown to have a marked effect on EV recovery following electroporation (Lennaárd et al., 2021).

Freeze-thaw cycling was found to be less effective for loading R6G compared to passive incubation (Figure 4a,b). Additionally, no significant change was observed in EV size distribution and concentration as measured by NTA in the freeze-thaw samples. Similar results were seen using freeze-thaw to load EVs with doxorubicin (Chen et al., 2023). On the other hand, others have shown that freeze-thaw cycles were more effective in loading catalase into EVs compared to incubation (Haney et al., 2015), which may be due to differences in the cargo properties.

Table 2 summarizes the major trends observed across the optimal conditions for each active loading method. We found that while sonication led to the greatest loading efficiency, electroporation led to the greatest number of loaded particles (Figure 5a,b). This difference highlights the significance of how loading is assessed, as well as how bulk versus single particle methods of measuring loading can lead to different conclusions. Single particle characterization also allows for investigation of differences in EV subpopulation loading. Differential loading across EV subpopulations may be due to differences in EV characteristics (e.g., lipids, sterols and size/morphology) as a result of disparate biogenesis pathways. Previously, it has been suggested that CD81<sup>+</sup>/CD9<sup>+</sup>/CD63<sup>-</sup> EVs are primarily ectosomes that originate via budding from the plasma membrane of the cell, while CD81<sup>-</sup>/CD9<sup>-</sup>/CD63<sup>+</sup> EVs are primarily exosomes originating from multivesicular bodies (Kowal et al., 2016; Mathieu et al., 2021). Therefore, slight changes in cell culture conditions may lead to large changes in the type and number of EVs secreted,

**TABLE 2** Major trends observed when comparing across active loading methods.

Read-out:	Comparison of loading methods:
Loading efficiency	Sonication > Electroporation > Freeze-thaw = Incubation
R6G particle number	Electroporation > Sonication = Incubation > Freeze-thaw = EV only
CFSE particle number	EV only > Incubation > Electroporation > Freeze-thaw > Sonication
CD63 particle number	EV only > Incubation = Electroporation > Freeze-thaw > Sonication
Total particle count by RPS	EV only = Freeze-thaw > Incubation = Sonication = Electroporation
Total particle count by NTA	Freeze-thaw > EV only = Incubation = Sonication = Electroporation

which is likely to have a large effect on loading. Furthermore, it should be noted that while sonication and electroporation were found to have significantly increased loading compared to the incubation control regardless of read-out (loading efficiency or R6G particle number), the increases were moderate. This highlights the challenges faced by the field of increase loading efficiency without damaging EVs.

Our data strongly suggest that CD63<sup>+</sup> EVs behave differently than other tetraspanin subpopulations during active loading. For example, in some cases, CD63 membrane expression was found to decrease without a commensurate decrease in total particle count. Similarly, prior work noted a decrease in CD63, CD24 and CD47 EV membrane expression after loading doxorubicin into EVs via extrusion, freeze-thaw, sonication and surfactant treatment (Chen et al., 2023). Additionally, with increased sonication, a significant increase in R6G-loaded CD81<sup>+</sup> and CD9<sup>+</sup> EV was observed but not in CD63<sup>+</sup> EVs (Figure 2c). These findings warrant further investigation into subpopulation-specific differences in active loading.

Shortcoming of our results is that our investigation is limited to only R6G without any functional readout assessed. The impact of the particular API properties was also not investigated in this study but also warrants further investigation. Considering that the API itself affects the loading mechanisms and efficiencies, it is likely that active loading methods need be optimized for each API specifically. For instance, electroporation has been found to cause siRNA to aggregate during the loading process (Kooijmans et al., 2013; Lamichhane et al., 2016). Furthermore, our results are limited to one EV source. Given our results suggesting that cell culture conditions are influencing secreted EVs and therefore loading, we hypothesize that testing loading in EVs from different source would likely lead to differences in loading results. Additionally, we did not study the effect of CFSE on the loading of R6G, which may have affected the loading of R6G in different ways depending on the loading methods used.

Finally, it should be noted that a large weakness of this study and indeed the field at large is the lack of calibrated methods to assess true size and concentration across the entire range of EVs. This study revealed major obstacles in comparing across techniques with different sensitivities. For example, some results could be explained by assuming that EVs break up into smaller particles (or release some or all cargo, resulting in a reduction in refractive index) below the NTA detection threshold but still detectable by interferometry or RPS. It is also possible that the lower detection limit of immunofluorescence precluded us from detecting EVs with low levels of R6G loaded. A lack of calibration for this instrument is severely limiting in this sense. While another fluorescence detection method, single particle flow cytometry, has been rigorously developed with size and fluorescence calibration routines, the technique is not suitable for analyzing EVs smaller than 90–100 nm on most cytometers, with the exception of newer instruments specialized for small particle analysis, thus miss the large majority of small EVs (Welsh et al., 2023). Our own cytometer routinely demonstrates a lower size limitation of >150 nm on a day-to-day basis, thus was not used for this study. Altogether, these limitations make interpreting orthogonal techniques exceeding difficult.

During this study, we observed inconsistencies in incubation replicates (Figure 6) this despite observing statistically significant differences between loading methods when using EVs from a single EV isolation (Figures 2–5). This highlights the challenges that the field will need to address for both large scale production and clinical translation of drug loaded EVs. In addition to incubation samples, inconsistencies were also observed between runs with active loading methods. Initially, CD63 particle count determine by tetraspanin capture assays was found to be significantly greater after three treatment cycles of sonication with pulsing compared to incubation but to be significantly less after electroporation with 25 V or 5 freeze-thaw cycles (Figures 2b, 3b and 4b). However, during the second run of the comparison study, sonication and freeze-thaw led to a significantly less CD63 particle count compared to incubation, while electroporation was not found to cause a significant change (Figure 5b). Again, this difference is likely due to differences in EVs from different isolations and slight differences in handling during loading. Differences between runs were also observed in R6G-loaded EV subpopulations. For instance, the relative number of CD63<sup>+</sup> R6G-loaded EVs was not significantly different between incubation and sonication samples for the first run (Figure 2c). However, during the comparison study the relative number of CD63<sup>+</sup> R6G-loaded EVs was significantly greater in the sonication samples compared incubation samples (Figure 5c). This difference is likely due to the above observed inconsistency in difference of CD63 particle count. These inconsistencies demonstrate the difficulty in developing a rigorous loading method that consistently target specific EV subpopulations given their high heterogeneity. Moreover, it highlights the importance in single particle level characterization

of the EV loading, as which subpopulations are loaded may greatly affect efficacy and can also be used to help tease out functional mechanisms (i.e., cellular uptake and longer circulation half-life).

Overall, despite these limitations, we have demonstrated (1) the importance of single particle characterization of EVs before and after loading with orthogonal methods for describing loading into EV subpopulations, (2) EV drug loading affect EV characteristics and (3) that the rigorous loading of API into the same subpopulations of EVs is challenging due to their dynamic nature. Our data also suggest that highly controlled and monitored cell culture conditions will be needed to ensure reproducibility of EVs, or the use of other methods to decrease the heterogeneity and/or increase the consistency of the EVs that will be loaded. In future, developing a robust loading method that achieve high loading in the same subpopulations of EV across multiple EV isolations should be developed for successful clinical translation of EV drug delivery systems.

## AUTHOR CONTRIBUTIONS

**Neona M. Lowe:** Conceptualization (equal); data curation (equal); formal analysis (equal); investigation (equal); methodology (equal). **Rachel R. Mizenko:** Formal analysis (equal); methodology (equal). **Bryan B. Nguyen:** Data curation (equal); methodology (equal). **Kwan Lun Chiu:** Formal analysis (equal); methodology. **Vishalakshi Arun:** Investigation (equal). **Alyssa Panitch:** Conceptualization (equal); data curation (equal); funding acquisition (equal); project administration (equal). **Randy P. Carney:** Conceptualization (equal); data curation (equal); formal analysis (equal); funding acquisition (equal); investigation (equal); methodology (equal); project administration (equal).

## ACKNOWLEDGEMENTS

The authors acknowledge support from the National Institutes of Health (NIH), including R01CA241666, R01EB033389 and R01EB034279. NL was supported by a National Institute of Heart, Lung, and Blood Institution (NHLBI) funded training grant programme (T32HL007013). RM was supported by 1F31NS120590. BN was supported by T32GM144303. This project was also supported by University of California Davis Biological Electron Microscopy (BioEM) Facility, which is supported by user fees, the Department of Molecular and Cellular Biology, the College of Biosciences, the Office of Research and the Provost's Office. The Technical Director, Dr. Fei Guo, is supported by discretionary funds provided by MCB. The K3 and DED detectors were purchased from funding support provided by the Department of Molecular and Cellular Biology, College of Biological Sciences and grant support provided by R00-GM080249 (J. Al-Bassam).

## CONFLICT OF INTEREST STATEMENT

The authors declare no conflicts of interest.

## DATA AVAILABILITY STATEMENT

All raw datasets generated and analyzed during the current study are freely available on a Zenodo repository with the identifier <https://doi.org/10.5281/zenodo.13274706>(link updated at final draft).

## ORCID

Neona M. Lowe  <https://orcid.org/0000-0002-7426-0273>

Randy P. Carney  <https://orcid.org/0000-0001-8193-1664>

## REFERENCES

- Alvarez-Erviti, L., Seow, Y., Yin, H., Betts, C., Lakhali, S., & Wood, M. J. (2011). Delivery of siRNA to the mouse brain by systemic injection of targeted exosomes. *Nature Biotechnology*, 29(4), 341–345. <https://doi.org/10.1038/nbt.1807>
- Artuyants, A., Chang, V., Reshef, G., Blenkiron, C., Chamley, L. W., Leung, E., & Hisey, C. L. (2021). Production of extracellular vesicles using a CELLline adherent bioreactor flask. In K. Turksen (ed.), *Bioreactors in stem cell biology* (Vol. 2436, pp. 183–192). Methods in Molecular Biology. Springer. [https://doi.org/10.1007/9781\\_2021\\_413](https://doi.org/10.1007/9781_2021_413)
- Bachurski, D., Schuldner, M., Nguyen, P. H., Malz, A., Reiners, K. S., Grenzi, P. C., Babatz, F., Schauss, A. C., Hansen, H. P., Hallek, M., & Pogge von Strandmann, E. (2019). Extracellular vesicle measurements with nanoparticle tracking analysis—An accuracy and repeatability comparison between NanoSight NS300 and ZetaView. *Journal of Extracellular Vesicles*, 8(1), 1596016. <https://doi.org/10.1080/20013078.2019.1596016>
- Buzas, E. I. (2022). The roles of extracellular vesicles in the immune system. *Nature Reviews Immunology*, Published online August 4, 2022. <https://doi.org/10.1038/s41577-022-00763-8>
- Caponnetto, F., Manini, I., Skrap, M., Palmari-Pallag, T., Di Loreto, C., Beltrami, A. P., Cesselli, D., & Ferrari, E. (2017). Size-dependent cellular uptake of exosomes. *Nanomedicine: Nanotechnology, Biology, and Medicine*, 13(3), 1011–1020. <https://doi.org/10.1016/j.nano.2016.12.009>
- Escudé Martínez de Castilla, P., Tong, L., Huang, C., Sofias, A. M., Pastorin, G., Chen, X., Storm, G., Schifferers, R. M., & Wang, J. W. (2021). Extracellular vesicles as a drug delivery system: A systematic review of preclinical studies. *Advanced Drug Delivery Reviews*, 175, 113801. <https://doi.org/10.1016/j.addr.2021.05.011>
- Chen, C., Li, Y., Wang, Q., Cai, N., Wu, L., & Yan, X. (2023). Single-particle assessment of six different drug-loading strategies for incorporating doxorubicin into small extracellular vesicles. *Analytical and Bioanalytical Chemistry*, 415(7), 1287–1298. <https://doi.org/10.1007/s00216-022-04248-4>
- Chen, C., Sun, M., Wang, J., Su, L., Lin, J., & Yan, X. (2021). Active cargo loading into extracellular vesicles: Highlights the heterogeneous encapsulation behaviour. *Journal of Extracellular Vesicles*, 10(13), e12163. <https://doi.org/10.1002/jev2.12163>
- Cooper, B. S., Hammad, L. A., & Montooth, K. L. (2014). Thermal adaptation of cellular membranes in natural populations of *Drosophila melanogaster*. *Functional Ecology*, 28(4), 886–894. <https://doi.org/10.1111/1365-2435.12264>

- Cooper, J. M., Wiklander, P. B., Nordin, J. Z., Al-Shawi, R., Wood, M. J., Vitlhani, M., Schapira, A. H., Simons, J. P., El-Andaloussi, S., & Alvarez-Erviti, L. (2014). Systemic exosomal siRNA delivery reduced alpha-synuclein aggregates in brains of transgenic mice. *Movement Disorders: Official Journal of the Movement Disorder Society*, 29(12), 1476–1485. <https://doi.org/10.1002/mds.25978>
- Donoso-Quezada, J., Ayala-Mar, S., & González-Valdez, J. (2020). State-of-the-art exosome loading and functionalization techniques for enhanced therapeutics: A review. *Critical Reviews in Biotechnology*, 40(6), 804–820. <https://doi.org/10.1080/07388551.2020.1785385>
- Elsharkasy, O. M., Nordin, J. Z., Hagey, D. W., de Jong, O. G., Schiffelers, R. M., Andaloussi, S. E., & Vader, P. (2020). Extracellular vesicles as drug delivery systems: Why and how? *Advanced Drug Delivery Reviews*, 159, 332–343. <https://doi.org/10.1016/j.addr.2020.04.004>
- Gehl, J. (2003). Electroporation: Theory and methods, perspectives for drug delivery, gene therapy and research. *Acta Physiologica Scandinavica*, 177(4), 437–447. <https://doi.org/10.1046/j.1365-201X.2003.01093.x>
- Haney, M. J., Klyachko, N. L., Zhao, Y., Gupta, R., Plotnikova, E. G., He, Z., Patel, T., Piroyan, A., Sokolsky, M., Kabanov, A. V., & Batrakova, E. V. (2015). Exosomes as drug delivery vehicles for Parkinson's disease therapy. *Journal of Controlled Release: Official Journal of the Controlled Release Society*, 207, 18–30. <https://doi.org/10.1016/j.jconrel.2015.03.033>
- Herrmann, I. K., Wood, M. J. A., & Fuhrmann, G. (2021). Extracellular vesicles as a next-generation drug delivery platform. *Nature Nanotechnology*, 16(7), 748–759. <https://doi.org/10.1038/s41565-021-00931-2>
- Hisey, C. L., Artuyants, A., Guo, G., Chang, V., Reshef, G., Middleditch, M., Jacob, B., Chamley, L. W., & Blenkinsop, C. (2022). Investigating the consistency of extracellular vesicle production from breast cancer subtypes using CELLLine adherent bioreactors. *Journal of Extracellular Biology*, 1(9), e60. <https://doi.org/10.1002/jex2.60>
- Hood, J. L., Scott, M. J., & Wickline, S. A. (2014). Maximizing exosome colloidal stability following electroporation. *Analytical Biochemistry*, 448, 41–49. <https://doi.org/10.1016/j.ab.2013.12.001>
- Jeppesen, D. K., Fenix, A. M., Franklin, J. L., Higginbotham, J. N., Zhang, Q., Zimmerman, L. J., Liebler, D. C., Ping, J., Liu, Q., Evans, R., Fissell, W. H., Patton, J. G., Rome, L. H., Burnette, D. T., & Coffey, R. J. (2019). Reassessment of Exosome Composition. *Cell*, 177(2), 428–445.e18. <https://doi.org/10.1016/j.cell.2019.02.029>
- Johnsen, K. B., Gudbergsson, J. M., Skov, M. N., Christiansen, G., Gurevich, L., Moos, T., & Duroux, M. (2016). Evaluation of electroporation-induced adverse effects on adipose-derived stem cell exosomes. *Cytotechnology*, 68(5), 2125–2138. <https://doi.org/10.1007/s10616-016-9952-7>
- Kamerkar, S., LeBleu, V. S., Sugimoto, H., Yang, S., Ruvio, C. F., Melo, S. A., Lee, J. J., & Kalluri, R. (2017). Exosomes facilitate therapeutic targeting of oncogenic KRAS in pancreatic cancer. *Nature*, 546(7659), 498–503. <https://doi.org/10.1038/nature22341>
- Kooijmans, S. A. A., Stremersch, S., Braeckmans, K., de Smedt, S. C., Hendrix, A., Wood, M. J. A., Schiffelers, R. M., Raemdonck, K., & Vader, P. (2013). Electroporation-induced siRNA precipitation obscures the efficiency of siRNA loading into extracellular vesicles. *Journal of Controlled Release: Official Journal of the Controlled Release Society*, 172(1), 229–238. <https://doi.org/10.1016/j.jconrel.2013.08.014>
- Kowal, J., Arras, G., Colombo, M., Jouve, M., Morath, J. P., Primdal-Bengtson, B., Dingli, F., Loew, D., Tkach, M., & Théry, C. (2016). Proteomic comparison defines novel markers to characterize heterogeneous populations of extracellular vesicle subtypes. *Proceedings of the National Academy of Sciences of the United States of America*, 113(8), E968–E977. <https://doi.org/10.1073/pnas.1521230113>
- Lamichhane, T. N., Jeyaram, A., Patel, D. B., Parajuli, B., Livingston, N. K., Arumugasamy, N., Schardt, J. S., & Jay, S. M. (2016). Oncogene knockdown via active loading of small RNAs into extracellular vesicles by sonication. *Cellular and Molecular Bioengineering*, 9(3), 315–324. <https://doi.org/10.1007/s12195-016-0457-4>
- Lamichhane, T. N., Raiker, R. S., & Jay, S. M. (2015). Exogenous DNA loading into extracellular vesicles via electroporation is size-dependent and enables limited gene delivery. *Molecular Pharmaceutics*, 12(10), 3650–3657. <https://doi.org/10.1021/acs.molpharmaceut.5b00364>
- Lennaard, A. J., Mamand, D. R., Wiklander, R. J., El Andaloussi, S., & Wiklander, O. P. B. (2021). Optimised electroporation for loading of extracellular vesicles with doxorubicin. *Pharmaceutics*, 14(1), 38. <https://doi.org/10.3390/pharmaceutics14010038>
- Mathieu, M., Névo, N., Jouve, M., Valenzuela, J. I., Maurin, M., Verweij, F. J., Palmulli, R., Lankar, D., Dingli, F., Loew, D., Rubinstein, E., Boncompain, G., Perez, F., & Théry, C. (2021). Specificities of exosome versus small ectosome secretion revealed by live intracellular tracking of CD63 and CD9. *Nature Communications*, 12(1), 4389. <https://doi.org/10.1038/s41467-021-24384-2>
- Mizenko, R. R., Brostoff, T., Rojalín, T., Koster, H. J., Swindell, H. S., Leiserowitz, G. S., Wang, A., & Carney, R. P. (2021). Tetraspanins are unevenly distributed across single extracellular vesicles and bias sensitivity to multiplexed cancer biomarkers. *Journal of Nanobiotechnology*, 19(1), 250. <https://doi.org/10.1186/s12951-021-00987-1>
- Pomatto, M. A. C., Bussolati, B., D'Antico, S., Ghiotto, S., Tetta, C., Brizzi, M. F., & Camussi, G. (2019). Improved loading of plasma-derived extracellular vesicles to encapsulate antitumor miRNAs. *Molecular Therapy Methods & Clinical Development*, 13, 133–144. <https://doi.org/10.1016/j.omtm.2019.01.001>
- Poupardin, R., Wolf, M., & Strunk, D. (2021). Adherence to minimal experimental requirements for defining extracellular vesicles and their functions. *Advanced Drug Delivery Reviews*, 176, 113872. <https://doi.org/10.1016/j.addr.2021.113872>
- Rajendran, R. L., Paudel, S., Gangadaran, P., Oh, J. M., Oh, E. J., Hong, C. M., Lee, S., Chung, H. Y., Lee, J., & Ahn, B. C. (2021). Extracellular vesicles act as nano-transporters of tyrosine kinase inhibitors to revert iodine avidity in thyroid cancer. *Pharmaceutics*, 13(2), 248. <https://doi.org/10.3390/pharmaceutics13020248>
- Silva, A. M., Lázaro-Ibáñez, E., Gunnarsson, A., Dhande, A., Daaboul, G., Peacock, B., Osteikoetxea, X., Salmond, N., Friis, K. P., Shatnyeva, O., & Dekker, N. (2021). Quantification of protein cargo loading into engineered extracellular vesicles at single-vesicle and single-molecule resolution. *Journal of Extracellular Vesicles*, 10(10), e12130. <https://doi.org/10.1002/jev2.12130>
- Théry, C., Witwer, K. W., Aikawa, E., Alcaraz, M. J., Anderson, J. D., Andriantsitohaina, R., Antoniou, A., Arab, T., Archer, F., Atkin-Smith, G. K., Ayre, D. C., Bach, J. M., Bachurski, D., Baharvand, H., Balaj, L., Baldacchino, S., Bauer, N. N., Baxter, A. A., Bebawy, M., ... Zuba-Surma, E. K. (2018). Minimal information for studies of extracellular vesicles 2018 (MISEV2018): A position statement of the International Society for Extracellular Vesicles and update of the MISEV2014 guidelines. *Journal of Extracellular Vesicles*, 7(1), 1535750. <https://doi.org/10.1080/20013078.2018.1535750>
- Van Niel, G., Carter, D. R. F., Clayton, A., Lambert, D. W., Raposo, G., & Vader, P. (2022). Challenges and directions in studying cell–cell communication by extracellular vesicles. *Nature Reviews Molecular Cell Biology*, 23(5), 369–382. <https://doi.org/10.1038/s41580-022-00460-3>
- Webber, J., & Clayton, A. (2013). How pure are your vesicles? *Journal of Extracellular Vesicles*, 2(1), 19861. <https://doi.org/10.3402/jev.v2i0.19861>
- Welsh, J. A., Arksteijn, G. J. A., Bremer, M., Cimorelli, M., Dignat-George, F., Giebel, B., Görgens, A., Hendrix, A., Kuiper, M., Lacroix, R., Lannigan, J., van Leeuwen, T. G., Lozano-Andrés, E., Rao, S., Robert, S., de Rond, L., Tang, V. A., Tertel, T., Yan, X., ... van der Pol, E. (2023). A compendium of single extracellular vesicle flow cytometry. *Journal of Extracellular Vesicles*, 12(2), e12299. <https://doi.org/10.1002/jev2.12299>
- Welsh, J. A., Goberdhan, D. C. I., O'Driscoll, L., Buzas, E. I., Blenkinsop, C., Bussolati, B., Cai, H., Di Vizio, D., Driedonks, T. A. P., Erdbrügger, U., Falcon-Perez, J. M., Fu, Q. L., Hill, A. F., Lenassi, M., Lim, S. K., Mahoney, M. G., Mohanty, S., Möller, A., Nieuwland, R., ... Witwer, K. W. (2024). Minimal information for studies of extracellular vesicles (MISEV2023): From basic to advanced approaches. *Journal of Extracellular Vesicles*, 13(2), e12404. <https://doi.org/10.1002/jev2.12404>
- Xi, X. M., Xia, S. J., & Lu, R. (2021). Drug loading techniques for exosome-based drug delivery systems. *Die Pharmazie*, 76(2), 61–67. <https://doi.org/10.1691/ph.2021.0128>



## SUPPORTING INFORMATION

Additional supporting information can be found online in the Supporting Information section at the end of this article.

**How to cite this article:** Lowe, N. M, Mizenko, R. R, Nguyen, B. B, Chiu, K. L., Arun, V., Panitch, A., & Carney, R. P. (2024). Orthogonal analysis reveals inconsistencies in cargo loading of extracellular vesicles. *Journal of Extracellular Biology*, 3, e70003. <https://doi.org/10.1002/jex2.70003>